Journal of Power Sources 234 (2013) 285–291

Contents lists available at SciVerse ScienceDirect

Journal of Power Sources

journal homepage: www.elsevier.com/locate/jpowsour

Hierarchically porous carbon nanofibers containing numerous heteroatoms for supercapacitors

Young Soo Yun [a], Changbin Im [a], Hyun Ho Park [a], Imgon Hwang [b], Yongsug Tak [b], Hyoung-Joon Jin [a,*]

[a] Department of Polymer Science and Engineering, Inha University, Incheon 402-751, Republic of Korea
[b] Department of Chemical Engineering, Inha University, Incheon 402-751, Republic of Korea

HIGHLIGHTS

- Hierarchically porous carbon nanofibers containing heteroatoms were prepared.
- Hierarchical structure was induced by controlling carbonization and activation of electrospun nanofibers.
- High specific energy (113 Wh kg^{-1}) and power (105 kW kg^{-1}) was achieved.
- A stable cycle life over 5000 cycles was also achieved.

ARTICLE INFO

Article history:
Received 29 November 2012
Received in revised form
28 January 2013
Accepted 30 January 2013
Available online 6 February 2013

Keywords:
Supercapacitor
Carbon nanofiber
Heteroatom
Activated carbon

ABSTRACT

In this study, hierarchically porous carbon nanofibers (HPCNFs) containing numerous electroactive heteroatoms are prepared by controlling carbonization and chemical activation. The HPCNFs have a large surface area of 2862.1 m^2 g^{-1}, hierarchical porous structure, and 20.6 at% electroactive oxygen atoms. These HPCNFs exhibit excellent electrochemical performance, and their thermal treatment with melamine results in nitrogen-doped HPCNFs (N-HPCNFs) with 9.1 at% nitrogen and improved electrical property ($1.8 \times 10^2\ \Omega\ \square^{-1}$). The electrochemical performance of N-HPCNFs is better than that of HPCNFs, displaying specific energy of 113 Wh kg^{-1}, specific power of 105 kW kg^{-1}, and stable cycle life of over 5000 cycles.

1. Introduction

The development of alternative energy storage/conversion devices with high power and energy densities has attracted considerable attention due to increasing concern over environmental issues and the depletion of fossil fuels. [1] Supercapacitors are promising devices for the quick storage of excess electrical energy [2,3] They have good reversibility, long cycle life, and substantial operational safety [1–4] In this context, supercapacitors are considered to be very attractive energy storage devices for application in electric vehicles, mobile phones, and uninterrupted power supplies for computers [1–4] However, supercapacitors are still not capable of realizing high energy densities comparable to those of lithium ion batteries, and this drawback restricts their adoption for these applications [1,5].

The energy density of a supercapacitor is dependent on the cell potential (V) and capacitance (C) as follows: $E = 1/2(CV^2)$ [3,5,6] Therefore, V and C need to be maximized to increase the energy density of a supercapacitor. Several strategies for achieving high C have been reported, which are mainly based on the use of pseudocapacitive electrode materials such as metal oxides and conductive polymers [7–10]. However, poor cycle stability, low electrical conductivity, and high cost have limited the practical application of these materials. Alternatively, carbon-based electrode materials containing numerous electroactive heteroatoms have been reported [11–15]. The incorporation of heteroatoms into carbon-based electrode materials has considerably improved specific capacitance and stabilized cycle performance. The heteroatoms induce pseudocapacitive behavior and improve the polar properties of carbon-based electrode materials. In addition, it has been demonstrated that carbon-based electrode materials are applicable for a wide range of potentials in an ionic liquid [16] This result is very encouraging for achieving high-energy-density

* Corresponding author.
E-mail address: hjjin@inha.ac.kr (H.-J. Jin).

0378-7753/$ – see front matter © 2013 Elsevier B.V. All rights reserved.
http://dx.doi.org/10.1016/j.jpowsour.2013.01.169

Table 1
Textural properties, and carbon, oxygen, and nitrogen contents of the samples.

Sample name	S_{BET} ($m^2\ g^{-1}$)	S_{MIC} ($m^2\ g^{-1}$)	S_{MESO} ($m^2\ g^{-1}$)	Carbon (at%)	Oxygen (at%)	Nitrogen (at%)
AC800	2488.8	1269.6	1219.2	74.6	25.4	–
AC1200	1920.1	342.3	1577.8	76.9	23.1	–
HPCNF800	2384.1	513.0	1871.1	82.9	13.5	3.6
HPCNF1200	2862.1	285.1	2577.0	78.4	20.6	1.0
N-HPCNF800	2074.8	683.9	1390.9	81.1	8.1	10.8
N-HPCNF1200	2527.7	246.5	2281.2	79.0	11.9	9.1

supercapacitors. With a high energy density, a supercapacitor must maintain its power density for large-scale applications such as electric vehicles. The power density of a supercapacitor is given by $P = V^2/(4R)$, where R is the equivalent series resistance (ESR) [3,6,17] This relation suggests that the resistivity of the electrode becomes the key factor in determining the power of the supercapacitor. Therefore, the design and fabrication of 3D nanoarchitectures from the appropriate nanoscale building blocks with the strategic use of void space and deliberate disorder as design components are important for optimizing energy storage and conversion [5,11,18–20] A hierarchical porous structure with minimized resistance and rapid electrolyte ion diffusion capability is required for creating a high-power-density supercapacitor [21–23].

In this study, we prepared highly porous carbon nanofibers by chemical activation of electrospun polyacrylonitrile (PAN) nanofibers. Interestingly, with an increase of the activation temperature, the pore structure changed from a micropore-dominant structure to a mesopore-dominant structure. Therefore, hierarchically porous carbon nanofibers (HPCNFs) were made by controlling the activation temperature. In addition, electroactive nitrogen groups were introduced onto the surfaces of the HPCNFs via thermal treatment with melamine. These HPCNFs containing numerous nitrogen atoms (N-HPCNFs) showed superior electrochemical performances, high specific energy and power, and good cycle stability.

2. Experimental

2.1. Electrospinning of PAN

10 wt% PAN (Sigma Aldrich, Mw = 150,000) solution was prepared in *N*,*N*-dimethylformamide (DMF). The PAN/DMF solution was placed in a syringe and ejected under 20–25 kV between the syringe needle and a rotating collector at a distance of 12 cm to form nanofibers.

2.2. Oxidative stabilization and KOH activation of electrospun PAN nanofibers

The prepared electrospun PAN nanofibers were stabilized at a heating rate of 1 °C min^{-1} at 280 °C for 2 h in air atmosphere. The stabilized nanofibers were soaked with KOH in water at a 1:2 w/w ratio (nanofibers/KOH) for 24 h. After soaking in KOH, the mixtures were dried in an oven at 80 °C for 24 h. Then, the mixtures were activated and carbonized at a heating rate of 5 °C min^{-1} and kept at 800 and 1200 °C for 2 h in Ar atmosphere. The activated and carbonized products were washed with distilled water several times to remove residual KOH, and then, the final products were dried in an oven at 80 °C for 24 h. The prepared samples are listed in Table 1. Activated carbons (ACs) were prepared by the same steps above, except for the electrospinning step. Furthermore, the activated carbon nanofibers were thermally treated with melamine, and are noted as N-HPCNFs (in the following section). The samples were named AC800, HPCNF800, and N-HPCNF800 (800 °C carbonization), and AC1200, HPCNF1200, and N-HPCNF1200 (1200 °C carbonization).

2.3. Preparation of N-HPCNFs

The HPCNFs of 100 mg were dispersed in *N*,*N*-dimethylformamide using ultrasound. Then, melamine monomer of 200 mg was added into the solution with vigorous stirring until it was completely dissolved. The HPCNFs/melamine mixture solutions were vacuum-filtrated and then vacuum-dried at 80 °C for 2 days. The mixtures were thermally treated at a heating rate of 5 °C min^{-1} and kept at 600 °C for 2 h in Ar atmosphere. The product was washed with ethanol several times and then dried in an oven at 80 °C for 24 h.

2.4. Characterization

The morphology of the fabricated ACs, HPCNFs, and N-HPCNFs were characterized by field emission scanning electron microscopy (FESEM, S-4300, Hitachi, Japan). The surface elemental compositions of ACs, HPCNFs, and N-HPCNFs were analyzed by X-ray photoelectron spectroscopy (XPS, AXIS-HIS, Kratos Analytical, Japan) with a dual-chromatic MgKα X-ray source at 1500 eV. The porous properties of ACs, HPCNFs, and N-HPCNFs were analyzed using nitrogen adsorption and desorption isotherms, which were obtained using a porosimetry analyzer (ASAP 2020, Micromeritics, USA) at −196 °C. Surface areas (S_{BET}) were calculated according to Brunauer–Emmett–Teller (BET) theory. The micropore surface area (S_{mic}) was

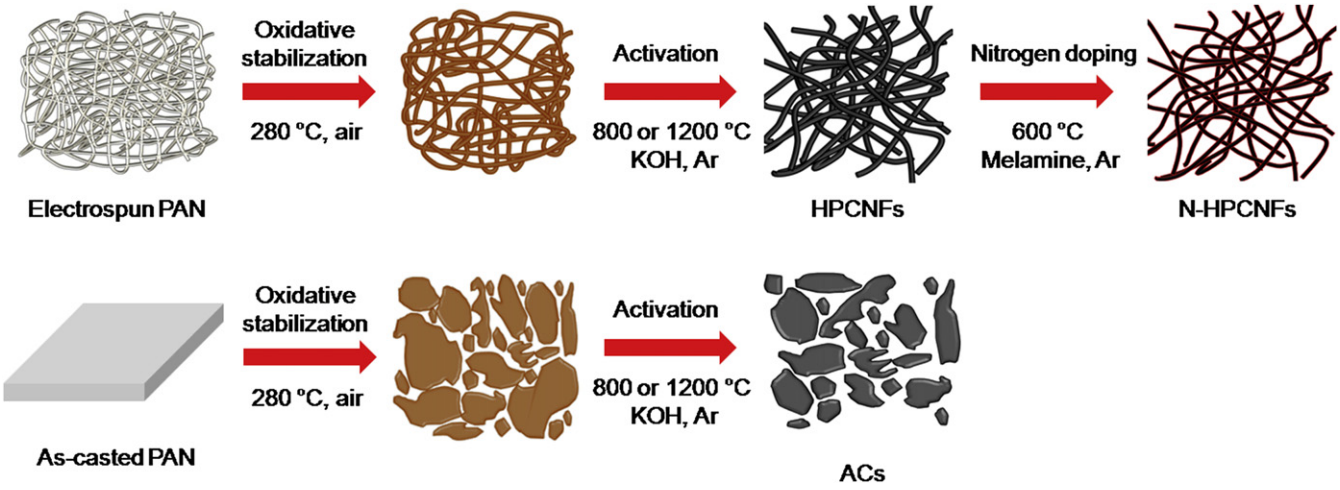

Fig. 1. Scheme for the processing of ACs, HPCNFs, and N-HPCNFs.

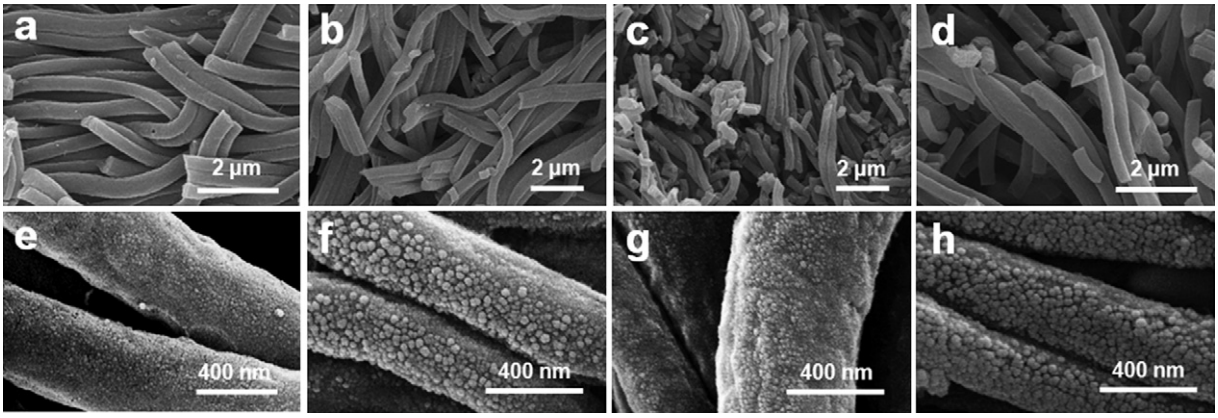

Fig. 2. SEM images of (a), (e) HPCNF800, (b), (f) HPCNF1200, (c), (g) N-HPCNF800, and (d), (h) N-HPCNF1200.

calculated according to the Horvath–Kawazoe (HK) method based on the t-plot theory, whereas the mesopore surface area (S_{meso}) was calculated based on the Barrett–Joyner–Halenda (BJH) theory. The working electrode was prepared via the following steps.

A two-electrode cell configuration was used to measure the electrochemical performances of the samples for use as electrodes for supercapacitors. For the aqueous system, 5 wt% polytetrafluoroethylene (PTFE, Sigma–Aldrich, 60 wt% dispersion in H_2O) was added to the samples as a binder. Typically, the sample and the PTFE were mixed into a paste using a mortar and pestle, then rolled into sheets of uniform thickness ranging from 40 to 50 μm (from sheet to sheet), which were then punched into 1-cm-diameter electrodes. For the non-aqueous system, the samples were mixed into a paste with 5 wt% of polyvinylidene fluoride.

The electrodes were formed from thick slurry and pressed onto conductive carbon-coated aluminum and nickel current collectors for the non-aqueous system and aqueous system, respectively. Each electrode had a diameter of 1 cm and thickness of approximately 100 μm. A typical pair of electrodes weighed 2.5–3.0 mg after drying overnight at 100 °C. 1 M H_2SO_4 (OCI company, 95%) was used as the aqueous electrolyte, and 1-butyl-3-methylimidazolium tetrafluoroborate (BMIM BF_4) as the non-aqueous electrolyte, which was obtained commercially from Sigma Aldrich and diluted with acetonitrile (AN) at a weight ratio of 1:1. A porous polypropylene separator (Whatman GF/D) was sandwiched between the electrodes in a stainless steel cell to form a fully assembled, two-electrode cell device. All steps in the cell preparation were carried out in an argon-filled glove box (oxygen and water contents, each below 1 ppm).

Electrochemical data were obtained using cyclic voltammetry, chronopotentiometry, and electrical impedance spectroscopy (EIS) (PGSTAT302N, Autolab). Capacitance, energy density, and power

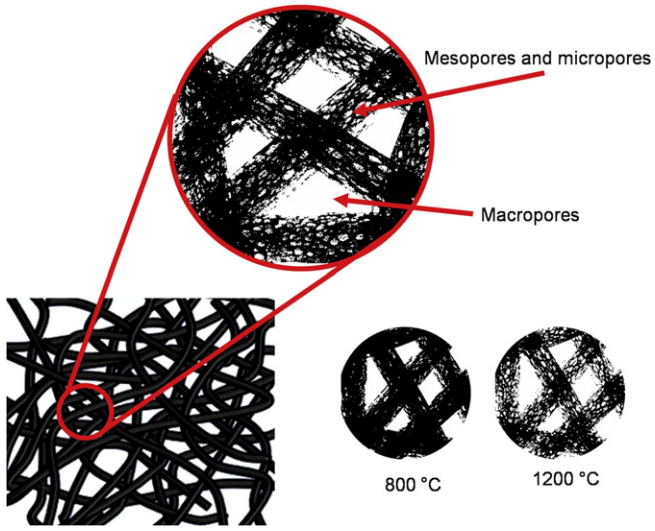

Fig. 3. Scheme showing the hierarchical structure of HPCNFs.

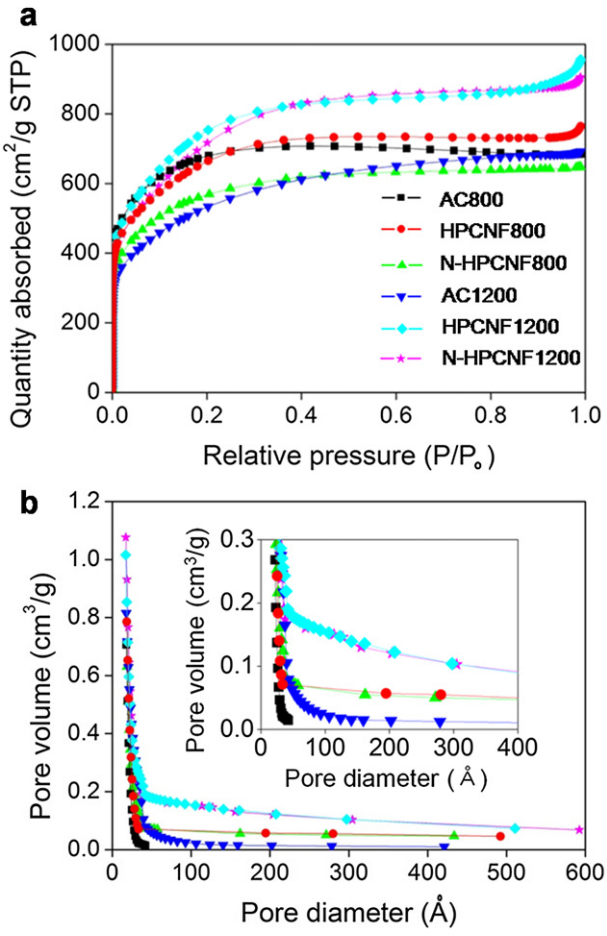

Fig. 4. (a) Nitrogen adsorption and desorption isotherm curves and (b) pore-size distributions of all the samples (black squares: AC800, red circles: HPCNF800, green triangles: N-HPCNF800, blue inverted triangles: AC1200, cyan diamonds: HPCNF1200, and magenta stars: N-HPCNF1200). (For interpretation of the references to color in this figure legend, the reader is referred to the web version of this article.)

density were all characterized by galvanostatic measurements. The current applied to the cells ranged from 0.1 to 50 A g^{-1}, while the potential between electrodes was swept between the cutoff values (0–1 V in the aqueous system, 0–3 V in the non-aqueous system). For the cycling test in both systems, 20 A g^{-1} was applied.

3. Results and discussion

As shown in Fig. 1, after the oxidative stabilization of the electrospun PAN nanofibers at 280 °C at a holding time of 2 h under air atmosphere, electrospun PAN nanofiber-KOH mixtures were thermally treated from room temperature to 800 and 1200 °C, respectively, at a holding time of 2 h under a heating rate of 10 °C min^{-1} and Ar flow of 200 ml min^{-1} for carbonization and activation. Nanofiber-like morphologies of the HPCNFs were maintained after carbonization and activation (Fig. 2a and c), and were not affected by the subsequent thermal treatment of the HPCNFs with melamine (Fig. 2b and d). The surfaces of all samples were very rough (Fig. 2e–h). In particular, the samples treated at 1200 °C were more activated and caved in (Fig. 2f and h). As a result, the hierarchically porous structure, composed of the macropores formed between their nanofiber-like structures and the surface meso-/micropores induced by KOH activation, was well developed in the HPCNFs and N-HPCNFs (Fig. 3). The pore characteristics of the samples are shown in Fig. 4. Nitrogen adsorption and desorption isotherms of all samples showed an IUPAC type-I microporous structure (Fig. 4(a)). The surface area of AC800 was 2488.8 m^2 g^{-1}, and the micropore to mesopore ratio was about 1, which means that the surface areas of micropores (1269.6 m^2 g^{-1}) and mesopores (1219.2 m^2 g^{-1}) were similar. In the case of AC1200, the surface area was 1920.1 m^2 g^{-1} and the micropore to mesopore ratio was 0.22. The micropore surface area was only 342.3 m^2 g^{-1}, while the mesopore surface area was 1577.8 m^2 g^{-1}. These results suggest that harsher activation conditions induce relatively larger pores through a stronger activation effect. This larger-pore tendency was also seen in the HPCNFs. However, HPCNFs had relatively lower micropore to mesopore ratios (0.27 in HPCNF800 and 0.11 in HPCNF1200), and the surface area of HPCNF1200 was larger than that of HPCNF800. This result is in contrast to that found in the case of ACs. In a mixture of electrospun PAN nanofiber and KOH, the activation agent can be evenly adsorbed onto the surface of the nanofiber, and activation progresses uniformly on all the surfaces. On the other hand, the activation in a bulk PAN film cast from a PAN/DMF solution progresses non-uniformly because the activation agent can be adsorbed only on bulk surfaces. Therefore, HPCNF800 had a wide activation area, and it was more strongly activated. However, for the 800 °C activation condition, the surface area of HPCNF800 was slightly lower than that of AC800 despite the wide range of activation of HPCNF800. This was due to the significantly low micropore area compared to the surface area. The mesopore and macropore volumes of HPCNFs were larger than those of ACs, because of the macropore formation by the aggregation of carbon nanofibers and mesopores, which was induced by the strong activation effects (Fig. 4(b)). Nevertheless, HPCNF1200 had the highest surface area of all the samples, suggesting that HPCNF1200 had the maximum activation. Furthermore, following thermal treatment with melamine, HPCNFs maintained their porous structure despite the introduction of numerous nitrogen heteroatoms on its surface. The physical properties of the samples are shown in Table 1.

Surface functional groups were analyzed by XPS. For HPCNF800, two distinct peaks (C–O centered at 286.0 eV and C(O)O centered at 288.5 eV) were visible in the C 1*s* spectra, as well as the main C–C peak at 284.7 eV (Fig. 5(a)). With KOH activation, numerous oxygen-containing functional groups were introduced on the surface of HPCNF800, and oxygen atoms existed as forms of the carbonyl groups (531.9 eV) and various other oxygen groups (533.5 eV, Fig. 5(b)). For HPCNF1200, two distinct peaks (C–O centered at

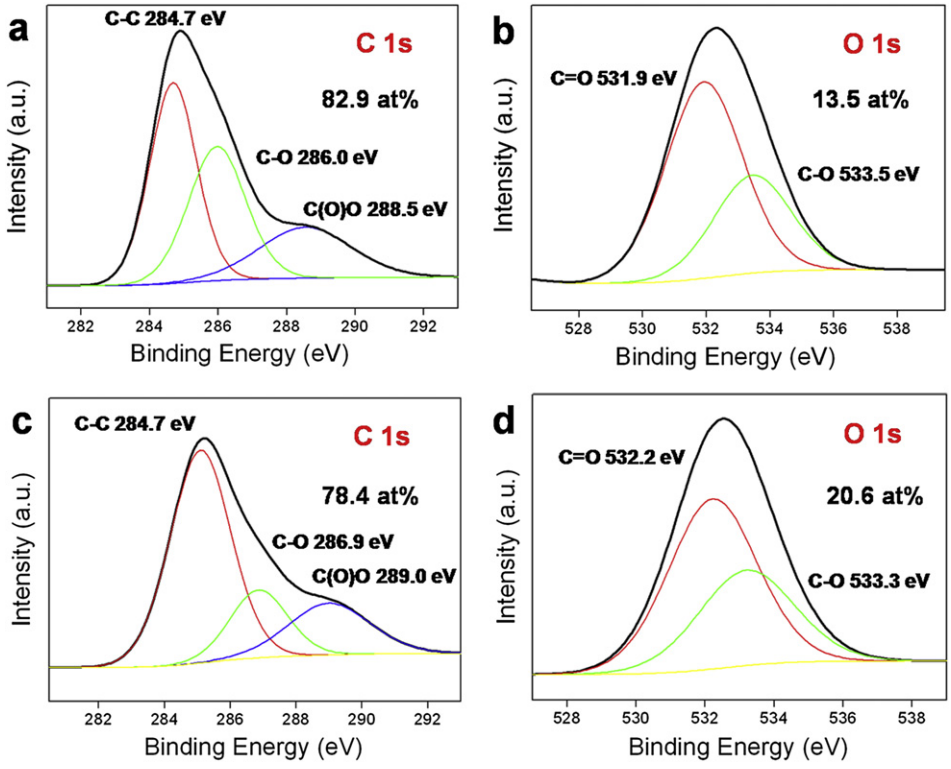

Fig. 5. XPS C 1*s* spectra of (a) HPCNF800 and (c) HPCNF1200, and XPS O 1*s* spectra of (b) HPCNF800 and (d) HPCNF1200.

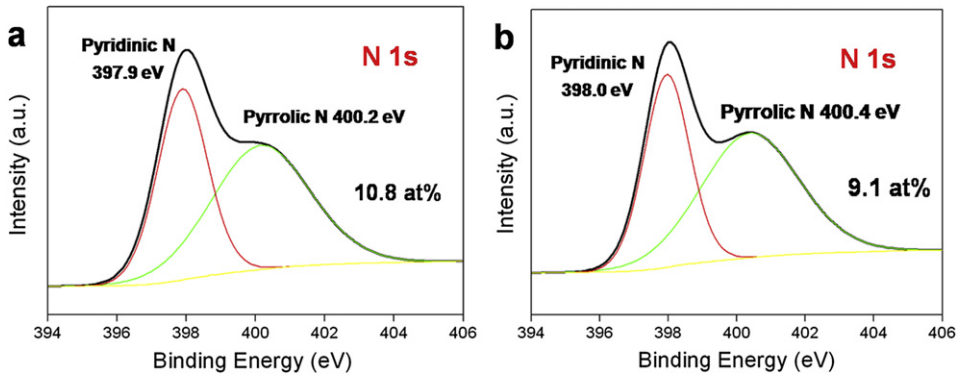

Fig. 6. XPS N 1*s* spectra of (a) N-HPCNF800 and (b) N-HPCNF1200.

286.9 eV and C(O)O centered at 289.0 eV) were seen in the C 1*s* spectra, in addition to the main C–C peak at 284.7 eV (Fig. 5(c)). Oxygen atoms of 20.6 at% were introduced on the surface of HPCNF1200, primarily as carbonyl groups (532.2 eV). Numerous nitrogen groups were also introduced on the surface of HPCNFs after thermal treatment with melamine. The nitrogen atoms in N-HPCNFs existed mainly as pyridinic and pyrrolic species (Fig. 6). These surface functional groups could provide extraordinary capacitance through Faradaic reactions for high-performance carbon materials, as well as improved electrode wettability because of the increased number of hydrophilic polar sites [11–15].

The electrochemical performances of the samples were analyzed using both an aqueous electrolyte, 1 M H_2SO_4, and an organic electrolyte, BMIM BF_4/AN. Fig. 7(a) shows the cyclic voltammograms of the samples in the aqueous electrolyte. The cyclic voltammogram curves of the HPCNFs are closer to rectangular shape than those of ACs, indicating the ideal capacitive behavior of the HPCNFs. The relatively steep slope of the cyclic voltammograms of HPCNFs at the switching potentials indicates a small mass-transfer resistance. This result suggests that the hierarchically porous structure facilitates ideal capacitive behavior as a result of rapid ionic motion. In addition, the cyclic voltammogram of HPCNF1200 exhibits a small hump, indicating that the capacitive response resulted from redox reactions. This hump in the cyclic voltammogramis is more pronounced in N-HPCNF1200. In addition, the capacitive areas of N-HPCNFs increased more than those of HPCNFs did. These results suggest that nitrogen groups could be more advantageous for pseudocapacitive effects. The rate capabilities of the samples are shown in Fig. 7(b). At scan rates from 5 to 100 mV s^{-1}, AC800 has capacitance retention of only 13%; HPCNF1200 with a hierarchical structure has capacitance retention of 45%. This value also surpasses that of AC1200 (26%). Fig. 7(c) shows the Nyquist plots of AC1200, HPCNF1200 and N-HPCNF1200 in a frequency range from 100 kHz to 0.1 Hz. Generally, the high-frequency region

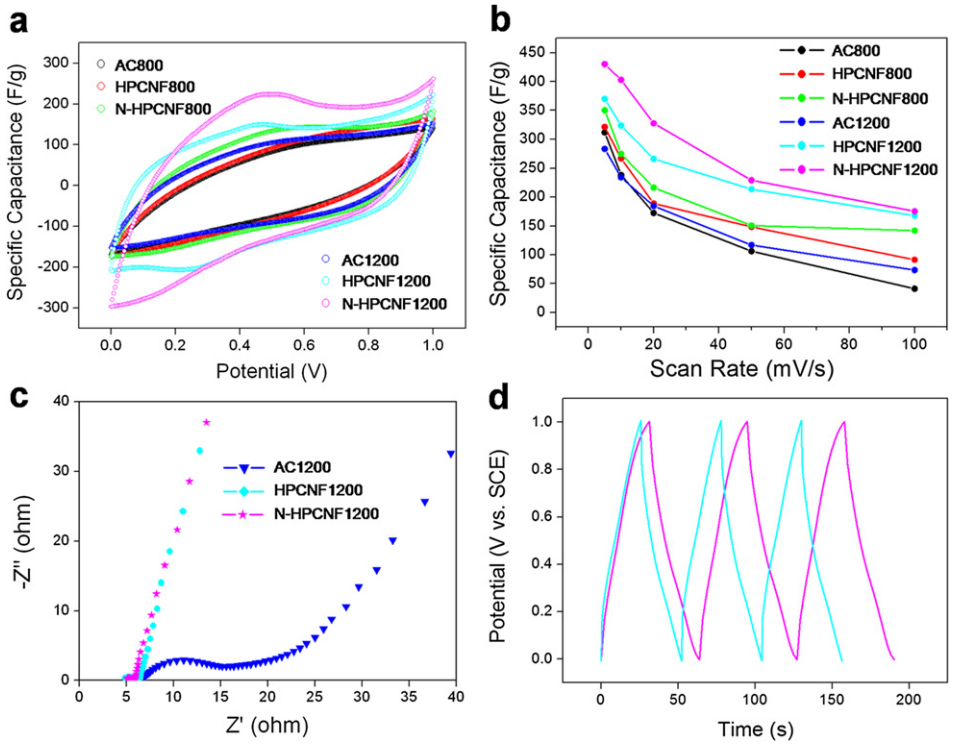

Fig. 7. (a) Cyclic voltammograms of all the samples at a scan rate of 5 mV s^{-1} over a potential range from 0 to 1 V in 1 M H_2SO_4 electrolyte, (b) specific capacitance of all the samples for different scan rates over a potential range from 0 to 1 V in 1 M H_2SO_4 electrolyte, (c) Nyquist plots of AC1200 (blue), HPCNF1200 (cyan) and N-HPCNF1200 (magenta) in the frequency range from 100 kHz to 0.1 Hz, and (d) galvanostatic charge/discharge curves of HPCNF1200 (cyan) and N-HPCNF1200 (magenta) over a potential range from 0 to 1 V in 1 M H_2SO_4 electrolyte. (For interpretation of the references to color in this figure legend, the reader is referred to the web version of this article.)

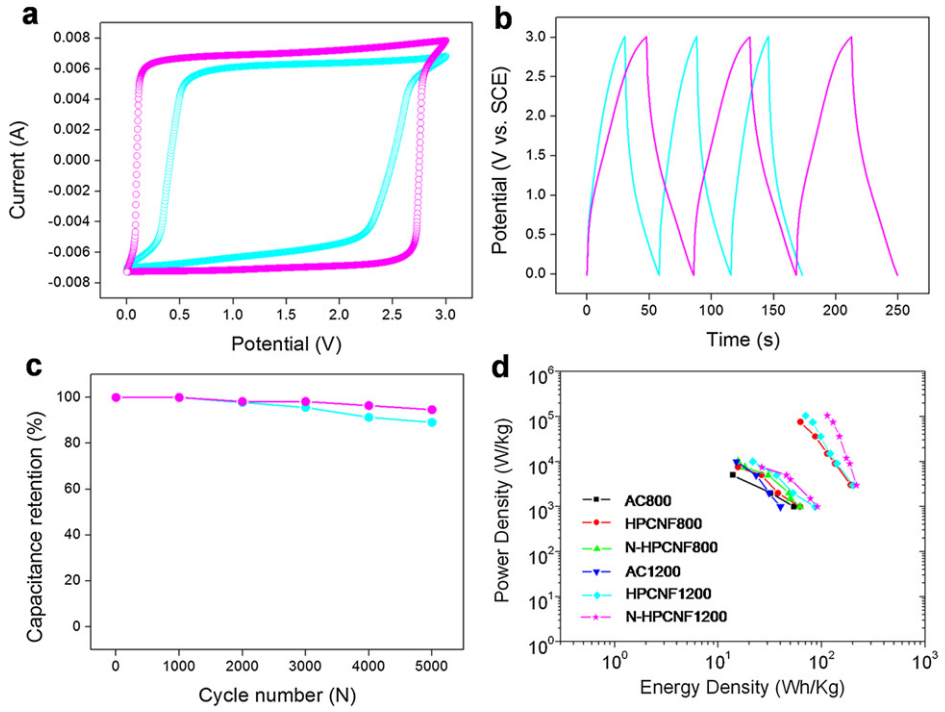

Fig. 8. (a) Cyclic voltammograms of HPCNF1200 (cyan) and N-HPCNF1200 (magenta) over a potential range from 0 to 3.0 V in the BMIM BF_4/AN electrolyte, (b) galvanostatic charge/discharge curves of HPCNF1200 (cyan) and N-HPCNF1200 (magenta) over a potential range from 0 to 3.0 V in the BMIM BF_4/AN electrolyte, (c) capacitance retentions of HPCNF1200 (cyan) and N-HPCNF1200 measured at a static current density of 20 A g^{-1} in the BMIM BF_4/AN electrolyte, and (d) the Ragone plots of all the sample-based supercapacitors in the BMIM BF_4/AN electrolyte and 1 M H_2SO_4 electrolyte.

of the Nyquist plot represents the sum of the internal resistance of the carbon material, the electrolyte resistance, and the contact resistance between the working electrode and the current collector. Under the same experimental conditions, resistance varied according to the internal resistance of the carbon material. The Nyquist plots of the samples show a semicircle at high frequencies (Fig. 7(c)). This semicircle is associated with the porous structure of the electrode and the Faradic charge-transfer resistance. The hierarchically porous structures of HPCNF1200 and N-HPCNF1200 increased pore accessibility. The real part of the impedance is then less frequency dependent, and the capacitive behaviors appear at lower resistance values than that of AC1200. In the low-frequency region, the imaginary component of the impedance plots represents the capacitive behavior. In the case of the EDLC, the impedance plot should theoretically be a vertical line parallel to the imaginary axis. However, the impedance plots of the samples with pseudocapacitive effects did not follow such a capacitive behavior. The N-HPCNFs also exhibited improved capacitance retention that was higher than that of ACs. Fig. 7(d) shows the galvanostatic charge/discharge curves of HPCNF1200 and N-HPCNF1200. The curves are nearly identical, exhibiting little IR drop despite the numerous heteroatoms. However, HPCNF1200 displayed lower capacitance than N-HPCNF1200 due to the enhanced pseudocapacitive effect from the nitrogen atoms.

Fig. 8(a) shows the cyclic voltammograms of HPCNF1200 and N-HPCNF1200 in the BMIM BF_4/AN electrolyte. The curve of N-HPCNF1200 exhibits typical capacitive behavior, with a rectangular shape from 0 to 3.0 V over a wide range of voltage scan rates. This rectangular shape is due to the electrochemical double layer capacitance (EDLC) without pseudocapacitive effects, which result from the Faradaic reactions leading to pseudocapacitance being limited to protic solvents [24–26] However, the curve of HPCNF1200 was slightly dented despite similar pore characteristics. A large amount of oxygen groups could have induced unfavorable effects in EDLC. The oxygen groups could have blocked the phase boundary between the electrode and electrolyte. Also, the electrical resistance characterized by the 4-probe method of HPCNF1200 ($2.1 \times 10^3\ \Omega\ \square^{-1}$) was higher than that of N-HPCNF1200 ($1.8 \times 10^2\ \Omega\ \square^{-1}$). The galvanostatic charge/discharge curves of HPCNF1200 and N-HPCNF1200 showed stable charge and discharge behaviors over a wide voltage range (Fig. 8(b)). Furthermore, HPCNF1200 had lower capacitance than N-HPCNF1200, which coincides with the cyclic voltammogram results. After 5000 constant current charge/discharge cycles at a current density of 20 A g^{-1} in the BMIM BF_4/AN electrolyte, the capacitance retentions of HPCNF1200 and N-HPCNF1200 were 89.8% and 94.6% of the initial capacitance, respectively, demonstrating their good cycle stability (Fig. 8(c)). The energy density and power density of all the samples are shown in Fig. 8(d). HPCNFs had higher specific energies and powers than ACs did because of the former's hierarchical structure. In addition, nitrogen doping of the HPCNFs improved both energy and power characteristics. The energy density and power density of the N-HPCNF1200 based supercapacitor reached 113 W h kg^{-1} and 105 kW kg^{-1}, respectively (Fig. 8(d)). This energy density is comparable to that of Li-ion batteries, and the power density is several orders of magnitude higher than that of Li-ion batteries because of the high capacitance and a wide potential window.

4. Conclusion

HPCNFs and N-HPCNFs were prepared, and their characteristics and electrochemical performances investigated in both aqueous electrolyte and ionic electrolyte. Harsher activation conditions (1200 °C activation) induced relatively larger pores and lower micropore to mesopore ratios than the 800 °C activation condition did. This stronger activation promoted rapid ionic motion. N-HPCNFs exhibited better electrochemical performance than

HPCNFs due to the pseudocapacitive effect of its nitrogen heteroatoms. N-HPCNFs also demonstrated superior electrical properties and stability, with high specific energy of 113 Wh kg^{-1}, specific power of 105 kW kg^{-1}, and stable cycle life of over 5000 cycles.

Acknowledgements

This work was supported by the National Research Foundation of Korea Grant funded by the Korean Government (MEST) (NRF-2010-C1AAA001-0029018)

References

[1] P. Simon, Y. Gogotsi, Nat. Mater. 7 (2008) 845–854.
[2] S. Aricò, P. Bruce, B. Scrosati, J. Tarascon, W.V. schalkwijk, Nat. Mater. 4 (2005) 366–377.
[3] L.L. Zhang, X.S. Zhao, Chem. Soc. Rev. 38 (2009) 2520–2531.
[4] Z. Liu, D. Yu, Neff A. Zhamu, B.Z. Jang, Nano Lett. 10 (2010) 4863–4868.
[5] G. Choi, M. Yang, W.H. Hong, J.W. Choi, Y.S. Huh, ACS Nano 6 (2012) 4020–4028.
[6] K.H. An, W.S. Kim, Y.S. Park, J.–M. Moon, D.J. Bae, S.C. Lim, Y.S. Lee, Y.H. Lee, Adv. Funct. Mater. 11 (2001) 387–392.
[7] Z.-S. Wu, D.-W. Wang, W. Ren, J. Zhao, G. Zhou, F. Li, H.-M. Cheng, Adv. Funct. Mater. 20 (2010) 3595–3602.
[8] S. Chen, J. Zhu, X. Wu, Q. Han, X. Wang, ACS Nano 4 (2010) 2822–2830.
[9] Q. Wu, Y. Xu, Z. Yao, A. Liu, G. Shi, ACS Nano 4 (2010) 1963–1970.
[10] X. Zhang, W. Shi, J. Zhu, D.J. Kharistal, W. Zhao, B.S. Lalia, H.H. Hng, Q. Yan, ACS Nano 5 (2011) 2013–2019.
[11] Y.S. Yun, J. Shim, Y. Tak, H.-J. Jin, RSC Adv. 2 (2012) 4353–4358.
[12] H.M. Jeong, J.W. Lee, W.H. Shin, Y.J. Choi, H.J. Shin, J.K. Kang, J.W. Choi, Nano Lett. 11 (2011) 2472–2477.
[13] D. Hulicova-Jurcakova, M. Seredych, G.Q. Lu, T.J. Bandosz, Adv. Funct. Mater. 19 (2009) 438–447.
[14] L. Zhao, L.-Z. Fan, M.-Q. Zhou, H. Guan, S. Qiao, M. Antonietti, M.-M. Titirici, Adv. Mater. 22 (2010) 5202–5206.
[15] Y.S. Yun, H.H. Park, H.–J. Jin, Materials 5 (2012) 1258–1266.
[16] Y. Zhu, S. Murali, M.D. Stoller, K.J. Ganesh, W. Cai, P.J. Ferreira, A. Pirkle, R.M. Wallace, K.A. Cychosz, M. Thommes, D. Su, E.A. Stach, R.S. Ruoff, Science 332 (2011) 1537–1541.
[17] C. Du, N. Pan, Nanotechnology 17 (2006) 5314–5318.
[18] R. Rolison, J.W. Long, J.C. Lytle, A.E. Fischer, C.P. Rhodes, T.M. McEvoy, M.E. Bourg, A.M. Lubers, Chem. Soc. Rev. 38 (2009) 226–252.
[19] Z. Xu, Z. Li, C.M.B. Holt, X. Tan, H. Wang, B.S. Amirkhiz, T. Stephenson, D. Mitlin, J. Phys. Chem. Lett. 3 (2012) 2928–2933.
[20] Y. Xiao, A. Zhang, S. Liu, J. Zhao, S. Fang, D. Jia, F. Li, J. Power Sources 219 (2012) 140–146.
[21] K. Xia, Q. Gao, J. Jiang, J. Hu, Carbon 46 (2008) 1718–1726.
[22] W. Xing, C.C. Huang, S.P. Zhuo, X. Yuan, G.Q. Wang, D. Hulicova-Jurcakova, Z.F. Yan, G.Q. Lu, Carbon 47 (2009) 1715–1722.
[23] R. Xu, Q. Cai, C. Zeng, D. Zou, F. Wu, X. Li, Y. Lu, R. Liang, J. Fu, Mater. Chem. 21 (2011) 1970–1976.
[24] L. Mayrand-Provencher, D. Rochefort, J. Phys. Chem. C 113 (2009) 1632–1639.
[25] R. Mysyk, E. Raymundo-Pinero, M. Anouti, D. Lemordant, F. Beguin, Electrochem. Commun. 12 (2010) 414–417.
[26] L. Timperman, H. Galiano, D. Lemordant, M. Anouti, Electrochem. Commun. 13 (2011) 1112–1115.